

Lawrence Berkeley National Laboratory

Lawrence Berkeley National Laboratory

Title

Surface reconstruction and chemical evolution of stoichiometric layered cathode materials for lithium-ion batteries

Permalink

<https://escholarship.org/uc/item/03z616h5>

Author

Lin, Feng

Publication Date

2014-04-15

Peer reviewed

This document was prepared as an account of work sponsored by the United States Government. While this document is believed to contain correct information, neither the United States Government nor any agency thereof, nor the Regents of the University of California, nor any of their employees, makes any warranty, express or implied, or assumes any legal responsibility for the accuracy, completeness, or usefulness of any information, apparatus, product, or process disclosed, or represents that its use would not infringe privately owned rights. Reference herein to any specific commercial product, process, or service by its trade name, trademark, manufacturer, or otherwise, does not necessarily constitute or imply its endorsement, recommendation, or favoring by the United States Government or any agency thereof, or the Regents of the University of California. The views and opinions of authors expressed herein do not necessarily state or reflect those of the United States Government or any agency thereof or the Regents of the University of California.

Surface Reconstruction and Chemical Evolution of $\text{LiNi}_x\text{Mn}_x\text{Co}_{1-2x}\text{O}_2$ Cathode Materials for Lithium-Ion Batteries

Feng Lin,^{1,*} Isaac Markus,^{1,2} Dennis Nordlund,³ Tsu-Chien Weng,³ [Mark Asta](#),² Huolin L. Xin,^{4,*} Marca M. Doeff¹

1. Environmental Energy Technologies Division, Lawrence Berkeley National Laboratory, Berkeley, CA 94720, USA

2. Department of Materials Science and Engineering, University of California, Berkeley, CA 94720, USA

3. Stanford Synchrotron Radiation Lightsource, SLAC National Accelerator Laboratory, Menlo Park, CA 94025, USA

4. Center for Functional Nanomaterials, Brookhaven National Laboratory, Upton, NY 11973, USA

All correspondence should be addressed F.L. (flin@lbl.gov) and H.L.X. (hxin@bnl.gov)

Abstract

The present study sheds light on the long-standing challenges associated with high-voltage operation of $\text{LiNi}_x\text{Mn}_x\text{Co}_{1-2x}\text{O}_2$ (NMC) cathode materials for lithium-ion batteries. Using correlated ensemble-averaged high-throughput synchrotron X-ray absorption spectroscopy and spatially resolved electron microscopy and spectroscopy, structural reconstruction (formation of a surface reduced layer, $R\bar{3}m$ to $Fm\bar{3}m$ transition) and chemical evolution (formation of a surface reaction layer) at the surface of NMC particles were directly observed. These are primarily responsible for the prevailing capacity fading and impedance buildup under high-voltage cycling conditions, as well as the first-cycle coulombic inefficiency. It was found, unexpectedly, that the surface reconstruction exhibits a strong orientation-dependent characteristic, which predominantly occurs along lithium diffusion channels. Furthermore, the surface reaction layer was found to be composed of lithium fluoride embedded in a complex organic matrix. This work represents a seminal study of surface reconstruction and chemical evolution in NMC materials using combined diagnostic tools, and indicates that strategically conformal surface functionalization on specific crystal orientations should be used to enhance the reliability of NMC materials operating in high-voltage batteries.

Keywords

Batteries, layered structure, surface reconstruction, chemical evolution, spectroscopy, microscopy

Introduction

Chemical evolution and structural transformations at the surface of a material directly influence characteristics relevant to a wide range of prominent applications including heterogeneous catalysis¹⁻³ and energy storage.^{4,5} Structural and/or chemical rearrangements at surfaces determine the way a material interacts with its surrounding environment, thus controlling the functionalities of the material.⁶⁻¹⁰ Specifically, the surfaces of lithium-ion battery (LIB) electrodes evolve simultaneously with charge-discharge cycling (i.e., *in situ* surface reconstruction, formation of a surface reaction layer) that can lead to deterioration of performance.^{4,5,11} An improved understanding of *in situ* surface reconstruction phenomena imparts knowledge not only for understanding degradation mechanisms for battery electrodes but also to provide insights into surface functionalization for enhanced cyclability.^{12,13}

The investigation of *in situ* surface reconstruction of layered cathode materials, such as $\text{LiNi}_x\text{Mn}_x\text{Co}_{1-2x}\text{O}_2$ (i.e., NMCs), lithium-rich $\text{Li}(\text{Li}_y\text{Ni}_{x-y}\text{Mn}_x\text{Co}_{1-2x})\text{O}_2$, lithium-rich/manganese-rich (composite layered-layered) $x\text{Li}_2\text{MnO}_3 \cdot (1-x)\text{LiMO}_2$ (M = Mn, Ni, Co, etc) materials, is technologically significant as they represent a group of materials with the potential to improve energy densities and reduce costs for plug-in hybrid electric vehicles (PHEVs) and electric vehicles (EVs).¹⁴⁻¹⁷ Practical implementation of some of these materials is thwarted by their high first-cycle coulombic inefficiencies,¹⁷⁻²⁰ capacity fading^{18,21} and voltage instability,²⁰⁻²² especially during high-voltage operation. Specifically, high-voltage charge capacities achieved in lithium-rich/manganese-rich layered cathodes are directly associated with various irreversible electrochemical processes including oxygen loss and concomitant lithium ion removal²³ and electrode/electrolyte reactions.²⁴ With respect to regular NMC materials, although improved high-voltage cyclability (2.0-4.7 V vs. Li^+/Li) was recently achieved when a small percentage of Co was substituted with Ti (< 4%), capacity fading still occurred after extended charge-discharge cycles.¹⁸ Due to the structural and chemical complexities of these layered structures, their fading mechanisms have not been fully resolved. Electron microscopy studies indicated that, in lithium and manganese-rich materials, the capacity fading and voltage decay were partially attributed to structural reconstruction inducing a transition from the layered structure to spinel and/or rock-salt structures at the

surface and/or in the bulk.^{5,17,25,26} A recent study investigated the atomic structure of Li_2MnO_3 after partial delithiation and re-lithiation to enable improved understanding of lithium-rich/manganese-rich materials.²⁷ However, these studies were mainly performed using spatially resolved techniques, thereby, inevitably lacking relevance to large-scale battery electrodes and failing to account for the inhomogeneous nature of battery electrodes.^{28–30} In addition, the role of electrode-electrolyte interactions in the surface reconstruction and chemical evolution has been rarely studied. The elucidation of the surface reconstruction of stoichiometric NMC materials should provide insights into the fading mechanisms not only for these compounds but also complement the mechanistic paradigm for more complex layered structures including lithium-rich and manganese-rich materials. In order to achieve a statistically viable and spatially visible elucidation (in real space) for surface phenomena on electrode materials, diagnostic techniques with complementary length scales should be implemented, including high-throughput synchrotron X-ray absorption spectroscopy (XAS) and atomic-scale scanning transmission electron microscopy (STEM) and electron energy loss spectroscopy (EELS).

Here, we report on the surface reconstruction and chemical evolution of stoichiometric NMC layered structures, using ensemble-averaged synchrotron XAS coupled with atomic-scale STEM-EELS, where the surface reconstruction and chemical evolution refer to the formations of surface reduced layer ($R\bar{3}m$ to $Fm\bar{3}m$ transition) and surface reaction layer (SRL), respectively. Our results reveal that the surface reconstruction occurs simultaneously with charge-discharge cycles and is strongly determined by the upper voltage limits used during cycling, electrolyte exposure, and crystal orientations. Furthermore, the major lithium-containing phase in the SRL is identified as lithium fluoride embedded in a complex amorphous organic matrix. The present study provides insights into the surface reconstruction and chemical evolution in NMC materials and directly illustrates the origin(s) of the long-standing challenges involved in cycling NMC materials to high voltages, such as capacity fading, impedance increases and first-cycle coulombic inefficiency. Finally, the study complements the mechanistic understanding of the surface reconstruction in layered materials and sheds light on the possible advantages of conformal functionalization on the surfaces of NMC particles.

Results

Characterization of pristine materials. $\text{LiNi}_{0.4}\text{Mn}_{0.4}\text{Co}_{0.18}\text{Ti}_{0.02}\text{O}_2$ (abbreviated NMC hereafter) powders with different particle size distributions were used for this study, because previous studies have shown that partial Ti-substitution in NMCs results in higher practical specific capacities, better capacity retention upon cycling to 4.7V vs. Li^+/Li , and decreased first cycle coulombic inefficiencies compared to baseline electrodes.^{18,19} The ratio of transition metals was verified to be close to stoichiometric $\text{LiNi}_{0.4}\text{Mn}_{0.4}\text{Co}_{0.18}\text{Ti}_{0.02}\text{O}_2$ (**Figure S1**). Extensive analysis was performed on the pristine materials to verify the homogeneity of the surface and bulk prior to electrochemical implementation. The combinatorial evaluation was done using a variety of X-ray and electron based techniques and is shown in **Figure 1**. The irregularly shaped primary particles of the NMC powder ranged in size from approximately 100-250 nm across (**Figure 1a**), indicating that the surface is terminated with various crystal orientations.

The specific surface area of the material was measured to be $9 \text{ m}^2/\text{g}$ by N_2 physisorption using the Brunauer-Emmett-Teller (BET) method (**Figure S2**). An extensive number of atomic-resolution annular dark-field STEM (ADF-STEM) images were obtained and representative ones are shown in **Figures 1b** and **1c**. STEM-EELS analysis was performed for the particle shown in **Figure 1b**, and it was found that the transition metal oxidation state remains constant from the surface to the bulk (**Figure S3**). Because ADF-STEM images approximately reflect the Z-contrast of materials, the images demonstrate that the material exhibits a well-defined layered structure, and the position of transition metals ($3b$ sites) are atomically resolved along the $[100]$ zone axis (**Figure 1c**). Note that lithium ($3a$ sites) and oxygen ($6c$ sites) are not visible in the Z-contrast ADF-STEM image due to their low atomic masses. Powder X-ray diffraction (XRD) confirmed that the NMC has the expected $R\bar{3}m$ layered structure (**Figure 1d**). The refined lattice parameters are consistent with those reported previously for this composition¹⁸ and are summarized in **Table S1**. Depth profiling of the electronic structure was carried out using XAS and STEM-EELS. Transition metal L-edge XAS and EELS measure the dipole allowed transitions from metal $2p$ orbitals to unoccupied metal $3d$ orbitals³¹⁻³³ and indirectly probe the local hybridization states for metal-oxygen

octahedral units³⁴ in an NMC material. Transition metal L-edge XAS is superior to K-edge XAS in terms of resolving local hybridization states, as the former directly probes the unoccupied $3d$ states in the metal $3d$ -oxygen $2p$ hybridized octahedral crystal field. Furthermore, L-edge XAS allows different sample depths to be probed from surface to bulk, depending on the detection modes. In the configuration used for this study, Auger electron yield (AEY), total electron yield (TEY) and fluorescence yield (FY) yield information about the chemical environments with depth sensitivities of 1-2 nm, 2-5 nm and 50 nm, respectively. Note that the FY probing depth is smaller than the particle size of the NMC materials, thus the signal primarily originates from the NMC particles on the top layer of the electrode rather than in the bulk of the composite electrode (typical thickness about 76 μm , **Figure S4**). XAS L-edge spectra of the transition metals exhibit almost identical shapes (e.g., $\text{Ni}3p_{3/2}$ and $\text{Ni}3p_{1/2}$ splitting features) and $L_{2,3}$ normalized intensities in AEY, TEY and FY modes (**Figure 1e**), which suggest an ensemble-averaged chemical homogeneity in the NMC material. Finally, the formal oxidation states of Ni, Mn and Co are determined to be +2, +4 and +3, respectively, as expected.^{31,35-37} Furthermore, the formal oxidation state of Ti is +4, and the shape of L-edge verifies the Ti substitution in the $R\bar{3}m$ layered lattice (**Figure S5**). A series of EELS area integrated spectra was recorded to directly assess the homogeneity of the chemical environment in a single NMC particle (**Figure 1f**) and representative ones are displayed in **Figure 1g**. The corresponding transition metal L-edge spectra exhibit no variation in the shapes or $L3/L2$ ratios at different probing positions. Furthermore, the O K-edge shows identical pre-edge peaks that are associated with the transitions from O $1s$ to O $2p$ -metal $3d$ hybridized states and are sensitive to the oxidation states of transition metals,^{38,39} which implies that the average oxidation states of transition metals remain constant from top surfaces to volumes deep in the bulk. The above ensemble-averaged and spatially resolved spectroscopic studies allow us to conclude that the pristine NMC material exhibits a well-defined $R\bar{3}m$ crystal structure with a homogenous distribution of the electronic structure. Furthermore, the homogeneity is not affected by the NMC particle size (**Figure S6**). Such comprehensive investigation of homogeneity is rarely reported in the literature, although its establishment is critical for resolving the effects of electrochemistry on surface reconstruction and chemical evolution.

Electrochemical tests of NMC materials. The electrochemical performances of the NMC materials were evaluated in lithium half-cells, and the cycled electrodes were collected for the subsequent synchrotron X-ray and electron spectroscopy based investigation. There are distinct differences in behavior between the high-voltage cycling (2.0-4.7 V) and lower-voltage cycling (2.0-4.3 V). [The NMC material shows a gradually sloping charge profile with no evidence of the high voltage plateau associated with irreversible loss of lithium and oxygen, commonly seen during electrochemical oxidation of lithium-excess compounds under these conditions.](#)^{16,22} Nevertheless, when repeatedly charged to 4.7V vs. Li⁺/Li, the capacity of the NMC electrode decreased with each cycle, while it fades very little during cycling between 2.0-4.3V (**Figures 2a-2c**). Furthermore, the potential hysteresis between lithium deintercalation (charging) and intercalation (discharging) increased gradually during high voltage cycling (indicated by the dashed arrows in **Figure 2a**); namely, larger overpotentials were observed for both processes. Because cycling was carried out between set voltage limits, this impedance rise also contributed to the apparent capacity fading. In contrast, capacity retention was much better when using a lower-voltage limit on charge, *i.e.*, when cycling between 2.0-4.3 V (**Figures 2b and 2c**). Such pronounced dependence on the voltage cutoff is partially caused by increased cell impedance under the high-voltage cycling conditions, as shown in **Figure 2d**. The Nyquist plots of the impedance data are composed of a semicircle at high frequencies and Warburg tails at low frequencies, which correspond to charge transfer resistance and mass transfer resistance, respectively. Both charge transfer resistance and mass transfer resistance markedly increased after the extended high-voltage cycling indicated by the increased semicircle radius and the decreased slope of Warburg tail (**Figure 2d**). In contrast, the charge transfer resistance slightly decreased after lower-voltage cycling between 2.0-4.3 V (**Figure 2d**), [which is likely attributed to cell conditioning and minimal surface reconstruction between 2.0-4.3 V \(discussed below\)](#). An impedance rise was also observed when the NMC electrode was exposed to the electrolytic solution for an extended period (**Figure 2e**) but not cycled. The similarities in the behavior suggest that the NMC electrodes undergo similar

modifications under conditions of cycling and electrolytic solution exposure, although to a lesser degree for the latter.

Post analysis of NMC materials. A correlated study using XAS, EELS and STEM imaging was performed to elucidate the mechanism of capacity fading and impedance rise in NMC cathodes under high-voltage cycling conditions. XAS/TEY is suitable for probing electronic structures at the top few nanometers due to the limited penetration depth of soft X-rays.⁴⁰ Because the measurements were performed on electrodes in the fully discharged state, nickel consistently showed a formal oxidation state of +2 after extended charge-discharge cycles (**Figure S7**). In contrast, manganese and cobalt underwent significant changes upon cycling. The contribution from the low-energy shoulders of Mn L3- and Co L3-edges grew gradually with increasing numbers of cycles (**Figures 3a** and **3b**), indicating an evolution of transition metal 3*d*-bands to higher occupancies, *i.e.*, reduced oxidation states.^{35,36,41} Furthermore, the oxidation states of transition metals exhibited depth-dependent characteristics, as shown by the direct comparison of AEY, TEY and FY spectra in **Figures 3c** and **3d**. The low-energy components of Mn L-edge and Co L-edge spectra were more obvious in the AEY mode than those in the TEY and FY modes. Therefore, the reduced Mn and Co species are primarily located at the surface. However, the high-energy component of the L3-edge was always present even in the surface-sensitive AEY mode, which suggests that the reduced Mn and Co species were not evenly distributed on individual NMC particles at the surfaces of the NMC electrodes. This observation coincides with previous studies that show that the charge distribution on the electrode surfaces is inhomogeneous in nature.³⁰ It is plausible that the reduced species were dominant on certain facets of individual NMC crystals, and that some surfaces exposed to incident X-rays retained the pristine electronic structure. Our subsequent investigation by ADF-STEM imaging further supports this hypothesis. An EELS line scanning profile was obtained on a particle cycled 5 times (**Figure 3e**). The variation of the Mn oxidation state along the scanning direction is evident by the blue shift of the absolute energy onset and the reduced L3/L2 ratio.³³ A calculation based on the linear combination of Mn²⁺ and Mn⁴⁺ was performed and the corresponding concentration profiles are presented in **Figure 3e (iv)**. The concentrations

of Mn^{2+} and Mn^{4+} were inversely correlated along the scanning direction, with Mn^{2+} primarily dominant on the surface. The thickness of the surface reduced layer was 2 nm for this particle, determined by using the intersections of Mn^{2+} and Mn^{4+} concentration profiles (**Figure 3e (iv)**). An equivalent experimental protocol was applied to an NMC particle cycled 20 times. Along the identical crystal orientation, the thickness of the surface reduced layer increased to approximately 3.4 nm (**Figure S8**). However, low-voltage cycling (2.0-4.3V) yielded a surface reduced layer with a thickness of 2 nm after 20 cycles (**Figure S9**). Another NMC material with identical composition yet smaller particle size was studied to probe the effect of particle size on the surface reduced layer, and the results show that the particle size imposes negligible effects on surface reduced layer within the range in this study (**Figure S10**), and had similar cycling behavior (**Figure S11**).

In addition to the surface reduced layer on the active NMC materials, a surface reaction layer (SRL) was observed after extended charge-discharge cycles (**Figure S12**). EELS revealed that the SRL consisted of a lithium fluoride (LiF) phase in a complex organic matrix (**Figure S12**). The SRL buildup is partially responsible for the impedance rise (**Figure 2d**). The emergence of the SRL is mainly attributed to the repeated high-voltage electrochemical processes, because it was barely observed in the electrode that was cycled to the low voltage (**Figure S13**) or exposed to the $\text{LiPF}_6/\text{EC-DMC}$ solution for 7 days, without being cycled (**Figure S14**).

The capacity retention of NMC materials is compromised when high-voltage cycling, such as 4.7 V vs. Li/Li^+ , is used. Here we show that the surface reduced layer is related to the inferior capacity retention observed under high-voltage cycling conditions. As shown in **Figures 4a** and **4b**, the relative amounts of reduced transition metals were higher after high-voltage cycling (2.0 – 4.7 V vs. Li/Li^+) than after lower-voltage cycling (2.0 – 4.3 V vs. Li/Li^+). These results suggest that the layered lattice is disrupted at high voltages resulting in a formation of a metastable phase that is readily reduced under discharging conditions. Presumably, the surface reduced layer creates a passivation layer (**Figure 4e**) that inhibits efficient lithium diffusion, thus adversely impacting capacity retention (**Figure 2d**). This hypothesis is further justified by several control experiments. First, after high-voltage cycling, the electrodes could not be revitalized to the initial state

by reassembling the cell with fresh electrolytic solution (**Figure S15a**), because this did not reduce the impedance (**Figure 2d**). Second, the capacity normally obtained with low-voltage cycling (2.0–4.3 V vs. Li/Li⁺) could not be restored after high-voltage cycling (**Figure S15b**). Third, the high-voltage capacity could be improved only by using an extremely slow charge/discharge rate even after 20 high-voltage cycles (**Figure S15c**). These observations indicate that the cycling losses imposed by high voltage cycling are mainly due to the impedance rise caused by the surface reduced layer and surface reaction layer rather than changes in the bulk electrode material.

Previous studies have attributed the surface reduced layer solely to electrochemical processes with little attention dedicated to the effects of electrode-electrolyte reactivity.^{4,5,17} Here we found that a surface reduced layer similar to the ones observed during high-voltage cycling is also created after an NMC electrode was immersed in the electrolyte (**Figures 4c and 4d**), although it is thinner. **In addition, its buildup leads to gradually increased charge transfer resistance (Figure 2e)**. After extended cycling, the surface reduced layer originates from dual effects involving both the electrode-electrolyte reactivity and electrochemical activation. The immediate generation of the reduced surface upon exposure to electrolyte may also be responsible for the first-cycle coulombic inefficiencies that are usually observed with NMC electrodes even when cycled conservatively, using voltage limits well below the oxidative stability limit of the electrolytic solution.

In the above discussion, XAS and EELS spectroscopies provided correlated evidence for the surface reduced layer and chemical evolution *via* the elucidation of local electronic structures primarily at the vicinity of NMC particle surfaces. The changes in electronic structures must be associated with the collapse and rearrangement of local crystal structures; i.e., lattice reconstruction. The atomic-resolution ADF-STEM imaging allows the visualization of the localized structural rearrangements at surfaces with the sensitivity of a single atom. A surface reconstruction layer is readily observed after the electrolyte exposure experiment (**Figure 5a**), where the dashed line indicates the boundary between the NMC R $\bar{3}m$ layered structure and the surface reconstruction layer. **This instantaneously generated reconstruction layer adversely impacts the capacity and first-cycle coulombic efficiency.** The crystal structure of the reconstruction layer consists

primarily of an $Fm\bar{3}m$ rock-salt structure (**Figure 5c**), with a few atomic layers of spinel structure as a “bridge” between the layered structure (containing Ni^{2+} , Mn^{4+} and Co^{3+}) and rock-salt structure (containing Ni^{2+} , Mn^{2+} and Co^{2+}). The thickness of the surface reconstruction layer increased after one complete cycle between 2.0-4.7 V (**Figure 5b**) relative to that observed on the particle that was exposed to the electrolytic solution without electrochemical cycling (although the duration of the two experiments was identical). The observation visually validates our previous conclusion that this layer originated from dual effects involving both electrode-electrolyte reactivity and electrochemical activation. By analyzing a large number of ADF-STEM images, we found that the surface reconstruction layer was greatly influenced by crystal orientations. **Figure 5e** shows a typical example of orientation-dependent surface reconstruction (more relevant images are available in the supplemental information, **Figure S16**). Furthermore, reconstruction-poor and -rich surfaces are occasionally observed on the same NMC particle after cycling (**Figure S16**). Due to the random orientation of NMC particles on the electrode surfaces, surface-sensitive XAS spectroscopy (i.e., AEY, TEY) yields an average of the electronic structures for reconstruction-poor and -rich surfaces, and thus the high-energy components of XAS/AEY and XAS/TEY are still present in the electrodes that have been cycled. In general, the thicker surface reconstruction layers are observed along lithium diffusion channels relative to other orientations (e.g., $\langle 001 \rangle$), suggesting that surface reconstruction is promoted by lithium removal during charging, and the reconstruction is more severe in the regions that undergo dynamic lithium transport. Interestingly, we also observed dangling layers (i.e., loose atomic layers) of the cubic rock-salt structure (indicated by blue arrows in **Figure 5f**) at the external surface of reconstruction layers. These loosely attached atomic layers are susceptible to dissolution into electrolytes and coincide with the suspected Mn^{2+} dissolution in a variety of Mn-containing cathodes⁴²⁻⁴⁴. It has been shown in **Figure S15c** that, after 20 high-voltage cycles, the discharge capacity could be nearly recovered at a slow rate (190 mAh/g, compared to the first cycle discharge capacity of 210 mAh/g). Therefore, the transition metal dissolution accounts for a capacity loss of no more than 20 mA/g.

Finally, we performed DFT calculation for the energy of formation for the rock salt structures from the layered structure as a function of lithium concentration (**Figure**

S17). Under oxygen partial pressure ranging from 10^{-12} atm to 1 atm we found that after about 40% of lithium has been removed from the NMC structure, it starts to become favorable to form the rock salt structure (i.e., negative formation energy). This supports the above results showing that the high-voltage cycling (i.e., more lithium ions are removed) leads to a much more severe buildup of the surface reduced layer (i.e., rock salt structure). Our experimental results showed that the $R\bar{3}m$ to $Fm\bar{3}m$ transition primarily occurred at the surface and direct exposure to electrolytic solution assisted the kinetics of the phase transition.

Discussion

We correlated cycling performance with the observation of structural reconstruction and chemical evolution at the surfaces of stoichiometric NMC materials using statistically viable high-throughput ensemble-averaged XAS as well as spatially resolved EELS and atomically resolved ADF-STEM imaging. The structural reconstruction was directly evidenced by the changes in the transition metal oxidation states and the atomic packing, which were achieved by synchrotron XAS and ADF-STEM, respectively. Our findings show that the challenge of achieving stable high-voltage cycling of the NMC electrodes lies with structural and chemical metastability at the surfaces. Upon cycling and/or electrolyte exposure, the surfaces of NMC particles undergo progressive reconstruction (i.e., lower transition metal oxidation states, **Figures 3a and 3b**) from an $R\bar{3}m$ layered structure to an $Fm\bar{3}m$ rock-salt structure in addition to the buildup of a complex surface reaction layer containing LiF and organic components (i.e., chemical evolution). These observations provide new insights into the capacity degradation and impedance buildup in stoichiometric NMC materials undergoing high-voltage cycling conditions. Interestingly, the structural reconstruction at the surface is highly crystal orientation dependent, and primarily occurs along the lithium ion transport direction. This phenomenon would have been omitted without such a study at complementary length scales. This finding suggests that conformal protection coatings on certain orientations of NMC particles should be more beneficial than those on other orientations provided that the conformal coating is capable of inhibiting surface reconstruction and allows for efficient lithium diffusion.

Methods

Preparation of electrode materials. $\text{LiNi}_{0.4}\text{Mn}_{0.4}\text{Co}_{0.18}\text{Ti}_{0.02}\text{O}_2$ materials were synthesized using a co-precipitation method. For the synthesis of $\text{LiNi}_{0.4}\text{Mn}_{0.4}\text{Co}_{0.18}\text{Ti}_{0.02}\text{O}_2$, 250 mL of an aqueous solution of transition metal nitrates (0.16 M $\text{Ni}(\text{NO}_3)_2$, 0.16 M $\text{Mn}(\text{NO}_3)_2$, 0.072 M $\text{Co}(\text{NO}_3)_2$), 0.008 M $\text{TiO}(\text{SO}_4)\cdot x\text{H}_2\text{O}$ and 250 mL of 0.8 M LiOH aqueous solution were dripped simultaneously into a beaker using a Masterflex C/L peristaltic pump and stirred continuously. The precipitate was collected, filtered and washed with DI water, and then dried overnight at 100 °C in the oven. The dried precipitate was ball-milled with LiOH or Li_2CO_3 and then heated in air at 900 °C for 3 h with a ramp of 2 °C/min. The use of Li_2CO_3 led to smaller NMC particles than that of LiOH. In the main text and supplementary information, the small and large NMC particles represent the materials made with Li_2CO_3 and LiOH, respectively.

Preparation of battery electrodes and electrochemical measurements. Composite electrodes were prepared with 84 wt% active material, 8 wt% polyvinylidene fluoride (Kureha Chemical Ind. Co. Ltd), 4 wt% acetylene carbon black (Denka, 50% compressed) and 4wt% SFG-6 synthetic graphite (Timcal Ltd., Graphites and Technologies) in N-methyl-2-pyrrolidinone and cast onto carbon-coated aluminum current collectors (Exopack Advanced Coatings (<http://www.exopackadvancedcoatings.com>) with typical active material loadings of 6-7 mg/cm². 2032 coin cells were assembled in a helium-filled glove box using the composite electrode as the positive electrode and Li metal as the negative electrode. A Celgard 2400 separator and 1 M LiPF_6 electrolyte solution in 1:2 w/w ethylene carbonate/dimethyl carbonate (Ferro Corporation) were used to fabricate the coin cells. Battery testing was performed on a computer controlled VMP3 potentiostat/galvanostat (BioLogic). 1C was defined as fully charging a cathode in 1 h, corresponding to a specific current density of 280 mA/g. Electrochemical impedance spectra were collected using a 10 mV AC signal ranging from 10mHz to 100 kHz using this same instrument. The electrodes were removed from coin cells, rinsed with dimethyl carbonate and dried in a helium-filled glove box for further study. The electrodes were sealed under helium and then transferred to the synchrotron beamline using a homemade

system to prevent air exposure. For electron microscopy and spectroscopy measurements, the electrode particles were scratched off and deposited onto TEM grids.

Materials Characterization. X-ray Diffraction (XRD) on powder samples was performed on a Bruker D2 Phaser diffractometer using $\text{CuK}\alpha$ radiation. Scanning electron microscopy (SEM) was performed on a JEOL JSM-7000F with a Thermo Scientific Inc. EDS (energy dispersive x-ray spectroscopy) detector.

XAS measurements were performed on the 31-pole wiggler beamline 10-1 at Stanford Synchrotron Radiation Lightsource (SSRL) using a ring current of 350 mA and a $1000 \text{ l}\cdot\text{mm}^{-1}$ spherical grating monochromator with $20 \mu\text{m}$ entrance and exit slits, providing $\sim 10^{11} \text{ ph}\cdot\text{s}^{-1}$ at 0.2 eV resolution in a 1 mm^2 beam spot. During the measurements, all battery electrode samples were attached to an aluminum sample holder using conductive carbon. Data were acquired under ultrahigh vacuum (10^{-9} Torr) in a single load at room temperature using total electron yield (TEY), Auger electron yield (AEY) and fluorescence yield (FY). The sample drain current was collected for TEY. Auger electron yield (AEY) was collected with a Cylindrical Mirror Analyzer using a pass energy of 200 eV and a kinetic energy window of 2 eV near the main Auger for oxygen and nitrogen, respectively. A silicon diode (IRD AXUV-100) was used to collect the fluorescence yield (FY) positioned near the sample surface. Contributions from visible light were carefully minimized before the acquisition, and all spectra were normalized by the current from freshly evaporated gold on a fine grid positioned upstream of the main chamber. XAS signals were collected at several positions on individual electrodes to ensure that data was representative of the sample.

A 200 keV and 300 keV probe-corrected field-emission scanning/transmission electron microscopes (S/TEM) were used for annular dark-field STEM (ADF-STEM) imaging and spatially resolved electron energy loss spectroscopy (EELS). Spectroscopic imaging was performed with an Enfina spectrometer on a Hitachi 2700C dedicated STEM.

The calculations were carried out using Kohn-Sham density functional theory with the projector augmented wave (PAW) method as implemented in the Vienna *ab*

initio Simulation Package (VASP). The calculation details are provided in the supplemental information.

References

1. Bell, A. T. The impact of nanoscience on heterogeneous catalysis. *Science* **299**, 1688–91 (2003).
2. Chen, M. S. & Goodman, D. W. The structure of catalytically active gold on titania. *Science* **306**, 252–5 (2004).
3. Cadigan, C. A. *et al.* Nanoscale (111) faceted rock-salt metal oxides in catalysis. *Catal. Sci. Technol.* **3**, 900 (2013).
4. Zheng, J. *et al.* Corrosion/Fragmentation of Layered Composite Cathode and Related Capacity/Voltage Fading during Cycling Process. *Nano Lett.* **13**, 3824–30 (2013).
5. Boulineau, A., Simonin, L., Colin, J.-F., Bourbon, C. & Patoux, S. First Evidence of Manganese-Nickel Segregation and Densification upon Cycling in Li-Rich Layered Oxides for Lithium Batteries. *Nano Lett.* **13**, 3857–63 (2013).
6. Toda, Y. *et al.* Activation and splitting of carbon dioxide on the surface of an inorganic electride material. *Nat. Commun.* **4**, 2378 (2013).
7. Chen, X., Liu, L., Yu, P. Y. & Mao, S. S. Increasing solar absorption for photocatalysis with black hydrogenated titanium dioxide nanocrystals. *Science* **331**, 746–50 (2011).
8. Doeff, M. M., Hu, Y., McLarnon, F. & Kostecki, R. Effect of Surface Carbon Structure on the Electrochemical Performance of LiFePO₄. *Electrochem. Solid-State Lett.* **6**, A207 (2003).
9. Stamenkovic, V. R., Mun, B. S., Mayrhofer, K. J. J., Ross, P. N. & Markovic, N. M. Effect of surface composition on electronic structure, stability, and electrocatalytic properties of Pt-transition metal alloys: Pt-skin versus Pt-skeleton surfaces. *J. Am. Chem. Soc.* **128**, 8813–9 (2006).
10. Lu, X. *et al.* New insight into the atomic structure of electrochemically delithiated O₃-Li(1-x)CoO₂ (0 ≤ x ≤ 0.5) nanoparticles. *Nano Lett.* **12**, 6192–7 (2012).
11. Jung, S.-K. *et al.* Understanding the Degradation Mechanisms of LiNi_{0.5}Co_{0.2}Mn_{0.3}O₂ Cathode Material in Lithium Ion Batteries. *Adv. Energy Mater.* n/a–n/a (2013). doi:10.1002/aenm.201300787

12. Leung, K. *et al.* Using atomic layer deposition to hinder solvent decomposition in lithium ion batteries: first-principles modeling and experimental studies. *J. Am. Chem. Soc.* **133**, 14741–54 (2011).
13. Zhang, X. *et al.* Structural and Electrochemical Study of Al₂O₃ and TiO₂ Coated Li_{1.2}Ni_{0.13}Mn_{0.54}Co_{0.13}O₂ Cathode Material Using ALD. *Adv. Energy Mater.* **3**, 1299–1307 (2013).
14. Nam, K.-W. *et al.* Combining In Situ Synchrotron X-Ray Diffraction and Absorption Techniques with Transmission Electron Microscopy to Study the Origin of Thermal Instability in Overcharged Cathode Materials for Lithium-Ion Batteries. *Adv. Funct. Mater.* **23**, 1047–1063 (2013).
15. Fell, C. R. *et al.* Correlation Between Oxygen Vacancy, Microstrain, and Cation Distribution in Lithium-Excess Layered Oxides During the First Electrochemical Cycle. *Chem. Mater.* **25**, 1621–1629 (2013).
16. Thackeray, M. M. *et al.* Li₂MnO₃-stabilized LiMO₂ (M = Mn, Ni, Co) electrodes for lithium-ion batteries. *J. Mater. Chem.* **17**, 3112 (2007).
17. Xu, B., Fell, C. R., Chi, M. & Meng, Y. S. Identifying surface structural changes in layered Li-excess nickel manganese oxides in high voltage lithium ion batteries: A joint experimental and theoretical study. *Energy Environ. Sci.* **4**, 2223 (2011).
18. Kam, K. C., Mehta, A., Heron, J. T. & Doeff, M. M. Electrochemical and Physical Properties of Ti-Substituted Layered Nickel Manganese Cobalt Oxide (NMC) Cathode Materials. *J. Electrochem. Soc.* **159**, A1383–A1392 (2012).
19. Kam, K. C. & Doeff, M. M. Aliovalent titanium substitution in layered mixed Li Ni–Mn–Co oxides for lithium battery applications. *J. Mater. Chem.* **21**, 9991 (2011).
20. Yu, H. & Zhou, H. High-Energy Cathode Materials (Li₂MnO₃–LiMO₂) for Lithium-Ion Batteries. *J. Phys. Chem. Lett.* **4**, 1268–1280 (2013).
21. Mohanty, D. *et al.* Structural transformation of a lithium-rich Li_{1.2}Co_{0.1}Mn_{0.55}Ni_{0.15}O₂ cathode during high voltage cycling resolved by in situ X-ray diffraction. *J. Power Sources* **229**, 239–248 (2013).
22. Thackeray, M. M., Wolverton, C. & Isaacs, E. D. Electrical energy storage for transportation—approaching the limits of, and going beyond, lithium-ion batteries. *Energy Environ. Sci.* **5**, 7854 (2012).
23. Armstrong, A. R. *et al.* Demonstrating oxygen loss and associated structural reorganization in the lithium battery cathode Li[Ni_{0.2}Li_{0.2}Mn_{0.6}]O₂. *J. Am. Chem. Soc.* **128**, 8694–8 (2006).

24. Jiang, M., Key, B., Meng, Y. S. & Grey, C. P. Electrochemical and Structural Study of the Layered, “Li-Excess” Lithium-Ion Battery Electrode Material $\text{Li}[\text{Li}_{1/9}\text{Ni}_{1/3}\text{Mn}_{5/9}\text{O}_2]$. *Chem. Mater.* **21**, 2733–2745 (2009).
25. Gu, M. *et al.* Formation of the spinel phase in the layered composite cathode used in Li-ion batteries. *ACS Nano* **7**, 760–7 (2013).
26. Tran, N. *et al.* Mechanisms Associated with the “Plateau” Observed at High Voltage for the Overlithiated $\text{Li}_{1.12}(\text{Ni}_{0.425}\text{Mn}_{0.425}\text{Co}_{0.15})\text{O}_{0.88}$ System. *Chem. Mater.* **20**, 4815–4825 (2008).
27. Wang, R. *et al.* Atomic Structure of Li_2MnO_3 after Partial Delithiation and Relithiation. *Adv. Energy Mater.* **3**, 1358–1367 (2013).
28. Chueh, W. C. *et al.* Intercalation pathway in many-particle LiFePO_4 electrode revealed by nanoscale state-of-charge mapping. *Nano Lett.* **13**, 866–72 (2013).
29. Harris, S. J. & Lu, P. Effects of Inhomogeneities—Nanoscale to Mesoscale—on the Durability of Li-Ion Batteries. *J. Phys. Chem. C* **117**, 6481–6492 (2013).
30. Kerlau, M., Marcinek, M., Srinivasan, V. & Kostecki, R. M. Studies of local degradation phenomena in composite cathodes for lithium-ion batteries. *Electrochim. Acta* **52**, 5422–5429 (2007).
31. Lin, F. *et al.* Origin of electrochromism in high-performing nanocomposite nickel oxide. *ACS Appl. Mater. Interfaces* **5**, 3643–9 (2013).
32. Lin, F. *et al.* Hole doping in Al-containing nickel oxide materials to improve electrochromic performance. *ACS Appl. Mater. Interfaces* **5**, 301–9 (2013).
33. Graetz, J., Ahn, C., Ouyang, H., Rez, P. & Fultz, B. White lines and d-band occupancy for the 3d transition-metal oxides and lithium transition-metal oxides. *Phys. Rev. B* **69**, 235103 (2004).
34. Van Veenendaal, M. & Sawatzky, G. Doping dependence of Ni 2p x-ray-absorption spectra of $\text{MxNi}_{1-x}\text{O}$ (M=Li,Na). *Phys. Rev. B* **50**, 11326–11331 (1994).
35. Gilbert, B. *et al.* Multiple Scattering Calculations of Bonding and X-ray Absorption Spectroscopy of Manganese Oxides. *J. Phys. Chem. A* **107**, 2839–2847 (2003).
36. Hy, S., Su, W.-N., Chen, J.-M. & Hwang, B.-J. Soft X-ray Absorption Spectroscopic and Raman Studies on $\text{Li}_{1.2}\text{Ni}_{0.2}\text{Mn}_{0.6}\text{O}_2$ for Lithium-Ion Batteries. *J. Phys. Chem. C* **116**, 25242–25247 (2012).

37. Yoon, W.-S. *et al.* Oxygen Contribution on Li-Ion Intercalation–Deintercalation in LiCoO₂ Investigated by O K-Edge and Co L-Edge X-ray Absorption Spectroscopy. *J. Phys. Chem. B* **106**, 2526–2532 (2002).
38. Hu, Z. *et al.* Hole distribution between the Ni 3d and O 2p orbitals in Nd_{2-x}Sr_xNiO_{4-δ}. *Phys. Rev. B* **61**, 3739–3744 (2000).
39. Yoon, W.-S. *et al.* Investigation of the Charge Compensation Mechanism on the Electrochemically Li-Ion Deintercalated Li_{1-x}Co_{1/3}Ni_{1/3}Mn_{1/3}O₂ Electrode System by Combination of Soft and Hard X-ray Absorption Spectroscopy. *J. Am. Chem. Soc.* **127**, 17479–17487 (2005).
40. Frazer, B. H., Gilbert, B., Sonderegger, B. R. & De Stasio, G. The probing depth of total electron yield in the sub-keV range: TEY-XAS and X-PEEM. *Surf. Sci.* **537**, 161–167 (2003).
41. Liang, Y. *et al.* Covalent hybrid of spinel manganese-cobalt oxide and graphene as advanced oxygen reduction electrocatalysts. *J. Am. Chem. Soc.* **134**, 3517–23 (2012).
42. Aurbach, D. *et al.* Capacity fading of Li_xMn₂O₄ spinel electrodes studied by XRD and electroanalytical techniques. *J. Power Sources* **81**, 472–479 (1999).
43. Goodenough, J. B. & Kim, Y. Challenges for Rechargeable Li Batteries. *Chem. Mater.* **22**, 587–603 (2010).
44. Zheng, H., Sun, Q., Liu, G., Song, X. & Battaglia, V. S. Correlation between dissolution behavior and electrochemical cycling performance for LiNi_{1/3}Co_{1/3}Mn_{1/3}O₂-based cells. *J. Power Sources* **207**, 134–140 (2012).

Acknowledgements

This work was supported by the Assistant Secretary for Energy Efficiency and Renewable Energy, Office of Vehicle Technologies of the U.S. Department of Energy under Contract No. DE-AC02-05CH11231 under the Batteries for Advanced Transportation Technologies (BATT) Program. The synchrotron X-ray portions of this research were carried out at the Stanford Synchrotron Radiation Lightsource, a Directorate of SLAC National Accelerator Laboratory and an Office of Science User Facility operated for the U.S. Department of Energy Office of Science by Stanford University. S/TEM and EELS experiments were performed at the Center for Functional

Nanomaterials, Brookhaven National Laboratory, which is supported by the U.S. Department of Energy, Office of Basic Energy Sciences under Contract No. DE-AC02-98CH10886, and at National Center for Electron Microscopy (NCEM) of the Lawrence Berkeley National Laboratory (LBNL), which is supported by the U.S. Department of Energy (DOE) under Contract No. DE-AC02-05CH11231.

Author contribution

F.L., I.M.M., H.L.X. and M.M.D. participated in conceiving and designing the experiments. F.L. performed materials syntheses, electrochemical measurements and prepared samples for materials characterization with assistance from I.M.M.. F.L., I.M.M., D.N. and T.C.W. performed synchrotron X-ray absorption experiments. H.L.X. performed S/TEM and EELS experiments. [I.M.M. performed DFT calculation under the supervision of M.A.](#) F.L. prepared the figures and wrote the manuscript with assistance from all authors. M.M.D. supervised the project. All authors participated in discussions and know the implications of the work.

LEGENDS

Figure 1 | Crystal structure and electronic structure of pristine NMC materials. (a) SEM image. (b) High-resolution Z-contrast ADF-STEM image. (c) Atomic resolution Z-contrast ADF-STEM image along the [100] zone axis, with the $R\bar{3}m$ $3a$ and $3b$ sites indicated in the image. (d) XRD pattern with Rietveld refinement (fitted parameters are given in **Table S1**). (e) XAS spectra of Ni L-edge (i), Mn L-edge (ii) and Co L-edge using Auger electron yield (blue), total electron yield (red) and fluorescence yield (green) modes. (f and g) EELS spectra integrated from areas (i), (ii), (iii) and (iv); [see also Figure S3 for the spectroscopic imaging of the pristine surface.](#)

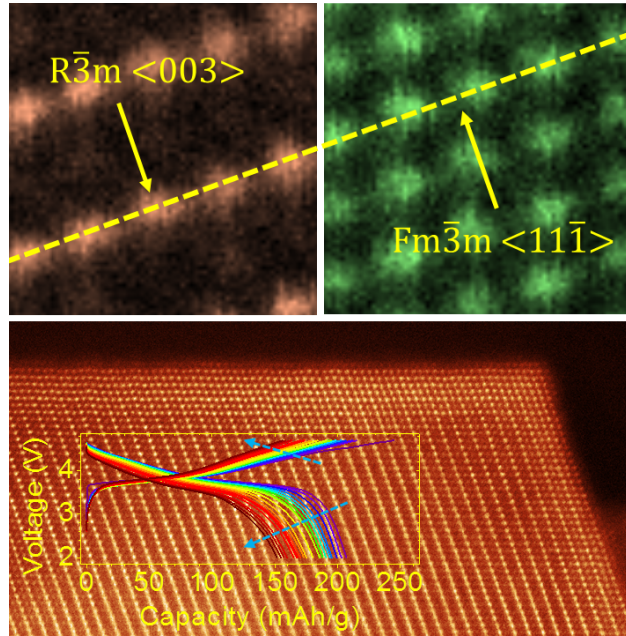
Figure 2 | Battery cycling performance of NMC materials. (a) Charge-discharge profiles at 2.0-4.7 V for 20 cycles at C/20, where the dashed arrows indicate the gradual capacity fading. (b) Charge-discharge profiles at 2.0-4.3 V for 20 cycles at C/20. (c) Charge and discharge capacities as functions of cycle number at 2.0-4.7 V (blue square) and 2.0-4.3 V (red circle), respectively. The solid and open data points represent charge and discharge capacities, respectively. (d) Nyquist plots of impedance data obtained on cells containing electrodes in the pristine state, cycled at 2.0-4.3 V for 20 cycles, cycled at 2.0-4.7 V for 20 cycles, and in the refreshed state (*i.e.*, rinsed with DMC, reassembled with fresh electrolyte after 20 cycles at 2.0-4.7 V). (e) A series of Nyquist plots for a pristine NMC electrode exposed to electrolytic solution for various periods up to 7 days. The exposure durations were 0 h (pristine), 5 h, 10 h, 1 day, 2 days, 3 days, 4 days, 5 days, and 7 days.

Figure 3 | Surface reconstruction and chemical evolution after charge-discharge cycles between 2-4.7 V vs. Li⁺/Li. (a) Mn L-edge XAS/TEY spectra and (b) Co L-edge XAS/TEY spectra after the designated number of cycles. (c) Mn L-edge XAS spectra and (d) Co L-edge XAS spectra for an electrode after 2 charge-discharge cycles in the AEY (blue), TEY (red) and FY (green) modes. (e) EELS line scan profile for an NMC particle along the <001> direction after 5 cycles: (i) STEM image for the scanning pathway, (ii) Mn L-edge EELS spectra along the scanning pathway, (iii) 2D EELS map visualizing the peak shift, and (iv) concentration profiles for Mn²⁺ and Mn⁴⁺ obtained from the data using a linear combination method. All the measurements were performed on electrodes in the fully discharged state.

Figure 4 | Dependence of surface reduced layer on cycling voltages and electrolyte exposure. (a) Mn L-edge XAS/TEY spectra and (b) Co L-edge XAS/TEY spectra of pristine and cycled electrodes (20 cycles). (c) Mn L-edge XAS/TEY/ FY spectra and (d) Co L-edge XAS/TEY/FY spectra of a pristine electrode and one exposed to electrolytic solution for 7 days. The blue dashed arrows in (a-d) indicate the increase of transition metals having low oxidation states. (e) Schematic model of a NMC particle with a surface reduced layer and a SRL.

Figure 5 | Atomic resolution ADF-STEM images of NMC particles. (a) After electrolyte exposure (the exposure time is approximately 30 hours, equivalent to the time used for one full cycle in this study). (b) After 1 cycle (2.0-4.7 V); the blue arrow indicates the surface reconstruction layer. (c and d) FFT results showing the surface reconstruction layer (Fm $\bar{3}$ m [110] zone axis) and the NMC layered structure (R $\bar{3}$ m [100] zone axis) respectively in (b). (e) Showing variation of the surface reconstruction layer thickness on orientation after 1 cycle (2.0-4.7 V). (f) Image showing loose atomic layers on an NMC particle, after 1 cycle (2.0-4.7 V). Dashed lines indicate the boundaries between the NMC layered structure and surface reconstruction layer in all images.

DISPLAY ITEMS



TOC

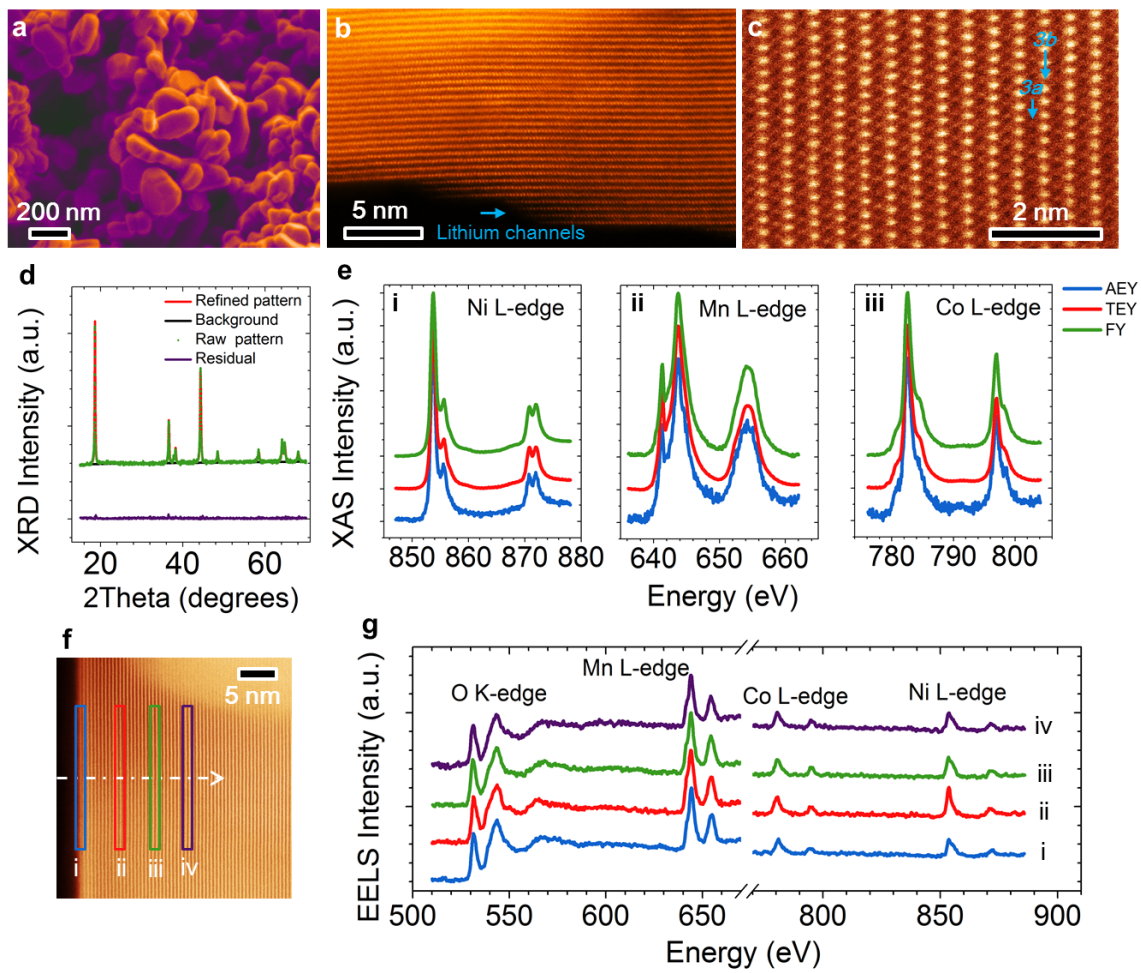


Figure 1

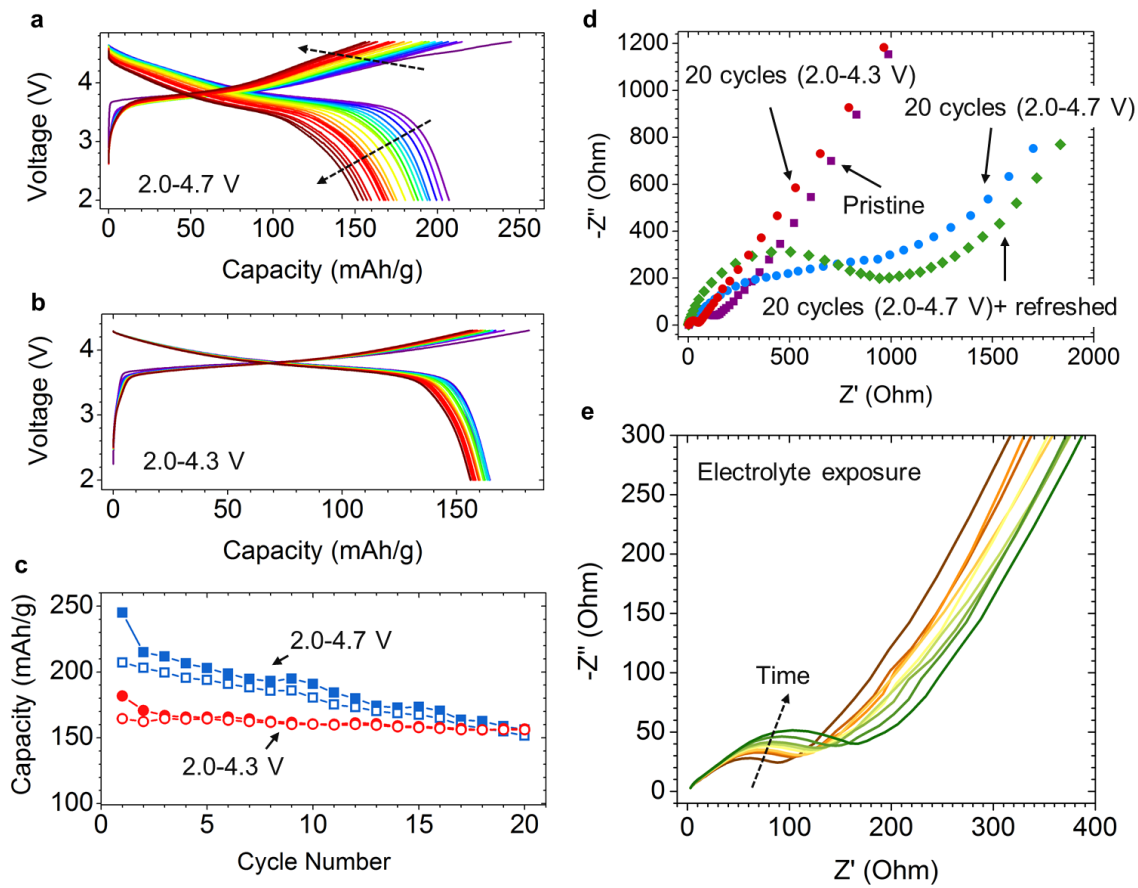


Figure 2

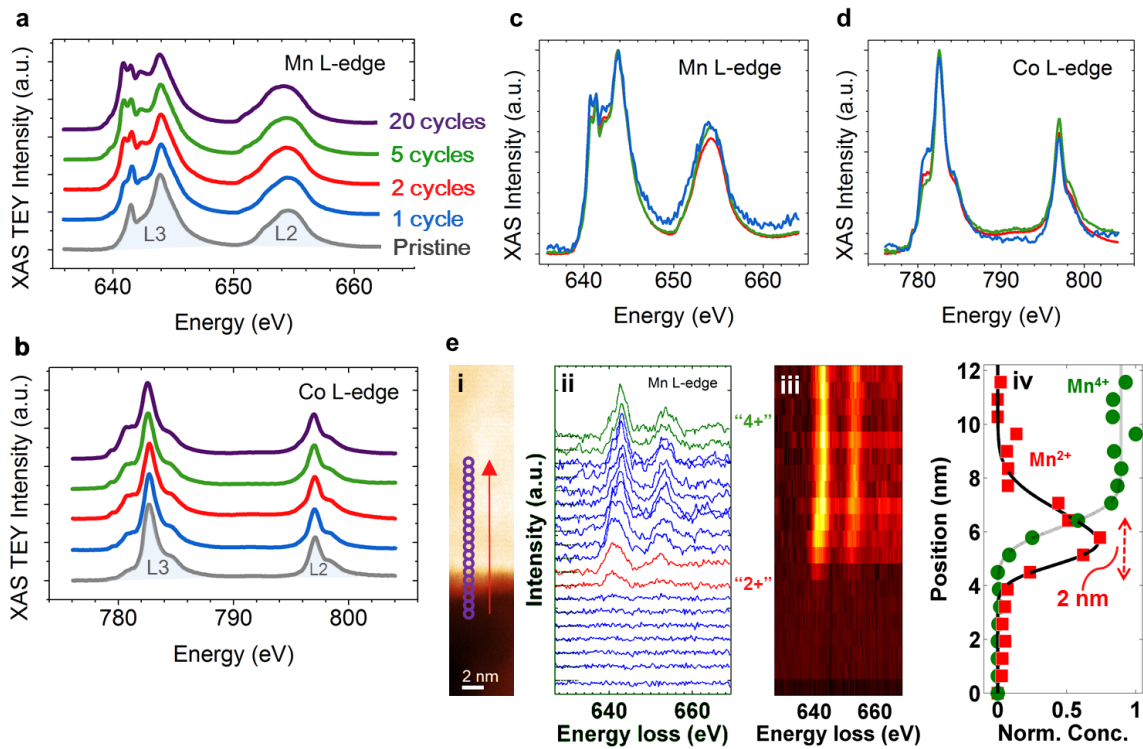


Figure 3

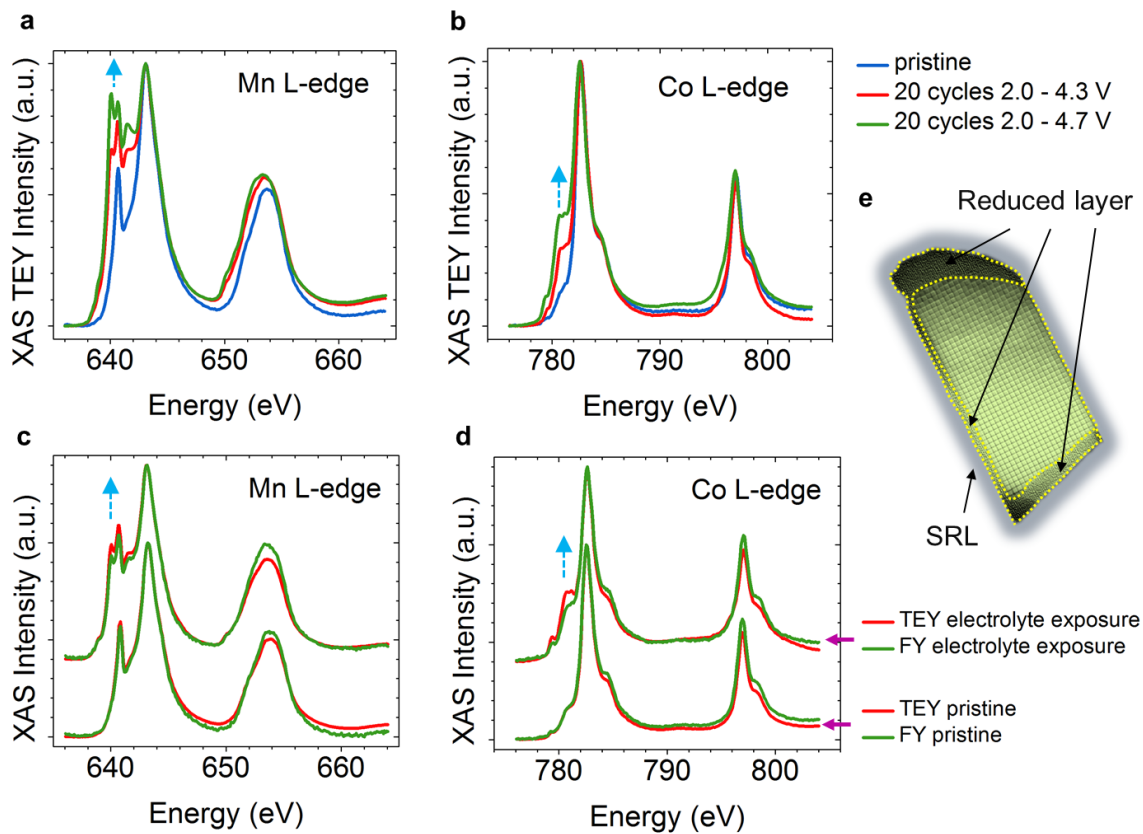


Figure 4

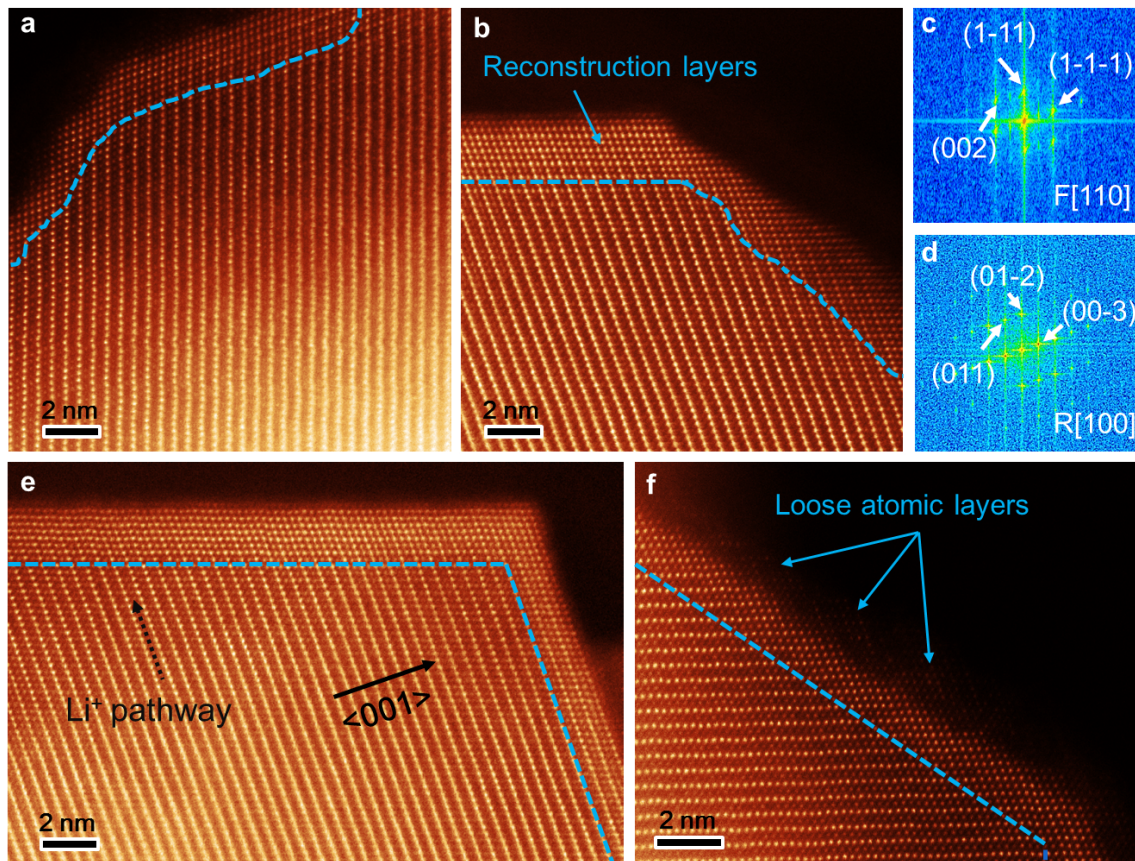


Figure 5